



## Article

# An Improved Vicarious Calibration Method Based on Multi-Grayscale Targets

Shiwei Bao <sup>1,2</sup>, Hongyao Chen <sup>1,\*</sup>, Yan Li <sup>3</sup>, Liming Zhang <sup>1</sup>, Wenxin Huang <sup>1</sup>, Xiaolong Si <sup>1</sup> , Xianhua Wang <sup>1</sup>, Zhou Fang <sup>3</sup>, Yuanwei Chen <sup>3</sup>, Xinrong Wang <sup>3</sup> and Xiaowen Zhao <sup>3</sup>

<sup>1</sup> Key Laboratory of Optical Calibration and Characterization, Hefei Institutes of Physical Science, Chinese Academy of Sciences, Hefei 230031, China

<sup>2</sup> Science Island Branch of Graduate School, University of Science and Technology of China, Hefei 230026, China

<sup>3</sup> State Key Laboratory of Space-Ground Integrated Information Technology Space Star Technology Company Ltd., Beijing 100095, China

\* Correspondence: hychen@aiofm.ac.cn

**Abstract:** Vicarious calibration is a well-developed method for electro-optical (EO) sensor calibration that has been used since the early 1980s. The radiometric calibration of reflectance solar band is mainly applied to reflection inversion. In this paper, a radiometric calibration-reflectance inversion (RCRII) model is proposed as an improved vicarious calibration method. Taking the reflectance of grayscale targets with constant spectrum, suitable uniformity, and near-Lambertian characteristics as the known information, the grayscale target calibration is realized, and the initial value of calibration coefficient and offset are calculated. Then, the adjacency effect is evaluated and corrected by reflectance inversion, and the results are fed back to the calibration process to realize the iterative process of calibration inversion rescaling. The results indicate that the absolute difference between the reflectance calculated with the RCRII model and measured reflectance is less than 0.01. By comparing with Sentinel-2A images, it is cross-verified that the difference of radiance between them is within 4%, and the absolute reflectance difference is less than 0.01, in the range of 0.1~0.3 reflectance.

**Keywords:** remote sensing; radiometric calibration; vicarious calibration



**Citation:** Bao, S.; Chen, H.; Li, Y.; Zhang, L.; Huang, W.; Si, X.; Wang, X.; Fang, Z.; Chen, Y.; Wang, X.; et al. An Improved Vicarious Calibration Method Based on Multi-Grayscale Targets. *Remote Sens.* **2022**, *14*, 3779. <https://doi.org/10.3390/rs14153779>

Academic Editors: Mohammadmehdi Saberioon and Daniel Spengler

Received: 27 June 2022

Accepted: 4 August 2022

Published: 6 August 2022

**Publisher's Note:** MDPI stays neutral with regard to jurisdictional claims in published maps and institutional affiliations.



**Copyright:** © 2022 by the authors. Licensee MDPI, Basel, Switzerland. This article is an open access article distributed under the terms and conditions of the Creative Commons Attribution (CC BY) license (<https://creativecommons.org/licenses/by/4.0/>).

## 1. Introduction

On-orbit calibration has the advantage of being performed under true flight conditions, rather than simulated flight-like conditions. The goals of on-orbit calibration are to measure parameters that cannot be measured on the ground, maintain calibration throughout a sensor's operational lifetime, quantify calibration uncertainty, and update calibration coefficients, if necessary, to meet measurement requirements [1]. It has been proven that the sensor response is affected by long-term attenuation and short-term fluctuation, particularly in the orbital environment during the on-orbit periods; if the calibration results are not continuously updated, it may lead to large errors [2,3]. On-orbit calibration includes onboard calibration, vicarious calibration, and other methods. Vicarious calibration can accomplish radiometric calibration based on actual Earth scenes, in order to realize a series of applications, such as reflectance inversion.

In recent years, scientists have developed a variety of solutions to effectively improve the calibration frequency and accuracy. For example, the Working Group on Calibration and Validation of the Committee on Earth Observation Satellites (CEOS-WGCV) has worked to establish a radiometric calibration network (RadCalNet). RadCalNet is a network of sites that can be used to compare different satellite sensors to each other and a common reference. It is based on the reflectance-based approach, with continuous deployment of automated instrumentation that is calibrated traceably to SI, as well as with known and peer-reviewed uncertainties [4,5].

In addition, pseudo-invariant site calibration realizes the high-frequency calibration of optical satellite sensors through the cross-calibration of MODIS, VIIRS, Landsat 8, and Sentinel 2 equipped with on-board calibration components. Due to the high reflectance of the on-board calibration diffuser, on-board calibration is usually realized at the high end of the sensor response, which is difficult for achieving high-precision calibration in the full dynamic range, and the low end of the response is a lack of verification. For example, although Landsat satellites have good consistency in at-sensor radiance/apparent reflectance, there are great differences in surface reflectance [6]. In addition to the influence of atmospheric aerosols, the sensor radiation response model (possibly with sensor offset) will be another potential reason. Therefore, full dynamic range high-frequency radiometric calibration is particularly urgent and important [7]. Based on the above reasons, full dynamic range and high-frequency calibration method based on grayscale targets are studied in this paper.

Continuous improvement of the spatial resolution of optical remote sensors enables on-orbit radiometric calibration based on grayscale targets. Robert E. Ryan of the NASA Stennis Space Center proposed a simplified approach to radiometric calibration. This new technique uses two neighboring uniform ground target areas with different reflectance values. For each target area, the radiance leaving the ground in the direction of the satellite is measured with a radiometrically calibrated spectroradiometer. Using the radiance measurements from the two targets, atmospheric adjacency and scattering effects can be subtracted. However, offsets, such as the dark current, atmospheric path radiation, and environmental radiation, are deducted as a whole, and each item cannot be separately determined.

In contrast, with remote sensor spatial resolution improvement, the adjacency effect has increasingly become one of the influencing factors that cannot be ignored. The adjacency effect is the image blur phenomenon caused by the entrance pupil of the remote sensor after atmospheric multiple scattering. The higher the remote sensor spatial resolution and larger the aerosol optical thickness are, the more serious the adjacency effect [8]. To date, the common adjacency effect correction methods include the Monte Carlo method and Fourier transform of the modulation transfer function (MTF) method [9], which are mostly used in atmospheric correction models. In addition, there has been much research regarding the adjacency effect based on three-dimensional radiative transfer. However, due to the massive computational efforts required to run three-dimensional radiative transfer codes, sophisticated atmospheric correction algorithms have not been pursued extensively [9]. Additionally, assuming that the surface and atmosphere are uniform in space, as well as only the vertical changes of atmospheric optical properties, the one-dimensional radiative transfer method implicitly explains the modeling of adjacency effect [10].

Based on the above, a radiometric calibration reflectance inversion iteration (RCRII) model is proposed in this paper. Firstly, the calibration coefficient and offset of the sensor can be calculated by using the multi-grayscale target calibration method. Then, the calculated parameters are substituted into the image for reflectance inversion, in order to evaluate the influence of adjacency effect. Finally, the results are fed back to the calibration process, so as to realize the radiometric calibration-reflectance inversion iteration method, which provides a new method for vicarious calibration.

The article is organized as follows: in Section 2, the RCRII model and data processing flow are introduced. Choosing the Pakistan remote sensing satellite (PRSS-1) as an example, the experimental data processing method is introduced in Section 3. In Section 4, PRSS-1 and Sentinel 2A are cross-verified and reflectance inversion verified, respectively, and their differences are compared. Finally, conclusions are provided in Section 5 and 6.

## 2. Radiometric Calibration-Reflectance Inversion Iterative Model

### 2.1. Radiometric Calibration Model

According to the atmospheric radiative transfer model, radiation information at the entrance pupil of the satellite sensor is shown in Figure 1, which mainly comprises the intrinsic atmospheric radiance, solar radiation reflected by the surface and directly transmit-

ted from the surface toward the sensor, and contribution of the environment, which reflects the total (direct and diffuse) downward flux. Photons reach the sensor via scattering.

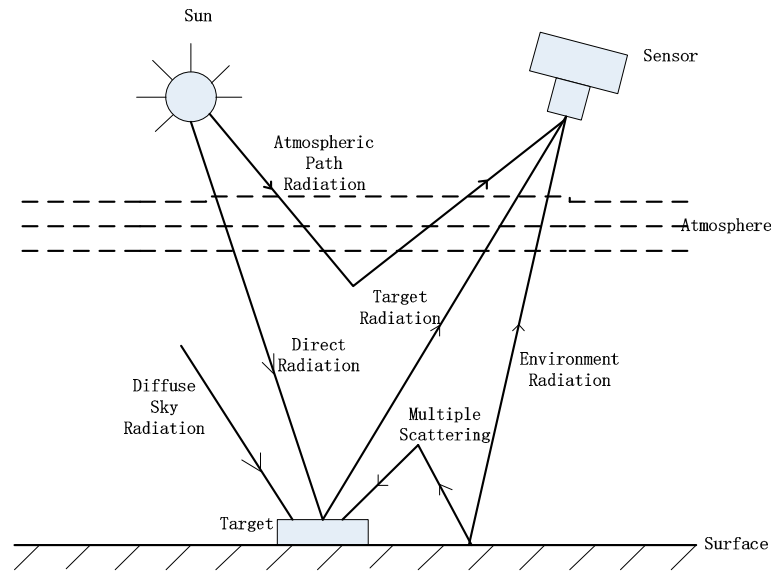


**Figure 1.** Schematic diagram of sun, target and sensor's reciprocity.

Assuming that the surface is uniform, the apparent reflectance collected by the optical sensor can be expressed as:

$$\rho^* = T_g \left[ \rho_a + \frac{\rho}{1 - s\rho} T(\theta_s) T(\theta_v) \right] \quad (1)$$

where  $\rho$  is the surface reflectance,  $T_g$  is the gaseous absorption transmittance,  $\rho_a$  is the path reflectance resulting from photons that never interact with the surface,  $s$  is the spherical albedo of the atmosphere,  $T(\theta_s)$  is the sun-to-ground total transmittance, i.e.,  $T(\theta_s) = e^{-\tau/\mu_s} + t_d(\theta_s)$ ,  $T(\theta_v)$  is the ground-to-sensor total transmittance, i.e.,  $T(\theta_v) = e^{-\tau/\mu_v} + t_d(\theta_v)$ ,  $e^{-\tau/\mu_s}$  is the sun-to-ground direct transmittance,  $t_d(\theta_s)$  is the sun-to-ground diffuse transmittance,  $e^{-\tau/\mu_v}$  is the ground-to-sensor direct transmittance, and  $t_d(\theta_v)$  is the ground-to-sensor diffuse transmittance.

When placing grayscale targets with different reflectance values as reference targets, considering that the target reflectance is inconsistent with that of the background, Equation (1) can be rewritten as:

$$\rho^* = T_g \left\{ \rho_a + \frac{T(\theta_s)}{1 - s \langle \rho \rangle} [e^{-\tau/\mu_v} \rho_t + t_d(\theta_v) \langle \rho \rangle] \right\} \quad (2)$$

where  $\rho_t$  is the target reflectance, and  $\langle \rho \rangle$  is not only the background reflectance but also the equivalent environmental reflectance affected by atmospheric multiple scattering, related to both the environmental and target reflectance. In the second simulation of the satellite signal in the solar spectrum (6S) radiative transfer model [11], the environmental function  $F(r)$  is used to characterize the contribution of the target reflectance to the background, which can be calculated as:

$$\langle \rho \rangle = F(r) \rho_t + (1 - F(r)) \rho_e \quad (3)$$

where  $\rho_e$  is the environmental reflectance,  $r$  is the target radius.

Combined with the camera radiometric calibration model  $DN = A \cdot \rho^* + DN_0$ , where  $DN$  is the camera digital number,  $DN_0$  is the camera offset, and  $A$  is the reflectance

calibration coefficient, it can be seen that the equation between the target reflectance and camera digital number is as follows:

$$DN = AT_g \frac{T(\theta_s)}{1 - s \langle \rho \rangle} e^{-\tau/\mu_v} \rho_t + AT_g [\rho_a + \frac{T(\theta_s)}{1 - s \langle \rho \rangle} t_d(\theta_v) \langle \rho \rangle] + DN_0 \quad (4)$$

Then, based on the linear regression between the target reflectance and digital value, the slope and intercept of the regression equation can be expressed as follows:

$$K = AT_g \frac{T(\theta_s)}{1 - s \langle \rho \rangle} e^{-\tau/\mu_v}. \quad (5)$$

$$b = AT_g [\rho_a + \frac{T(\theta_s)}{1 - s \langle \rho \rangle} t_d(\theta_v) \langle \rho \rangle] + DN_0 \quad (6)$$

where  $K$  is the slope of the linear regression, and  $b$  is the intercept of the linear regression.

Another consideration here is that, as mentioned above, the equivalent environmental reflectance is related to the target reflectance. Then, for different reflectance targets, the equivalent environmental reflectance cannot be regarded as a constant, which may lead to nonlinear error. This phenomenon will be analyzed later.

When comparing the grayscale target calibration method to the traditional vicarious calibration method, the following two points should be considered:

(1) When the calibration experiment is conducted at a uniform site, it is necessary to mark the position of the measurement area to obtain the digital number of the corresponding area in the image [12]. The grayscale target is small, easy to identify, and exhibits a suitable uniformity. This approach reduces the random measurement error in the process of reflectance linear regression, and the measurement accuracy is, thus, generally higher than that of the traditional vicarious calibration method.

(2) When the sensor observes the Earth, there may occur nonlinear, stray light, or dark current issues. The single-point calibration method can hardly eliminate this factor. Assuming that the offset is 0, the site with low reflectance will lead to a large error in the calculated calibration coefficient. Based on grayscale targets, the calibration coefficient and offset can be calculated according to the slope and intercept equation.

## 2.2. Reflectance Inversion Model

Based on Equations (5) and (6), the initial values of the reflectance calibration coefficient  $A$  and offset  $DN_0$  can be obtained. When these values are applied to the image, the apparent reflectance of the whole image can be obtained. The surface reflectance of the image area can be determined through reflectance inversion. Based on the 6S atmospheric correction model and adjacency effect analysis, a reflectance inversion model is proposed in this paper. The inversion steps are as follows:

(1) In regard to atmospheric absorption and atmospheric path radiation correction of the apparent reflectance image, Equation (2) can be rewritten as:

$$\frac{\rho^*}{T_g} - \rho_a = \frac{T(\theta_s)}{1 - s \langle \rho \rangle} e^{-\tau/\mu_v} \rho_t + \frac{T(\theta_s)}{1 - s \langle \rho \rangle} t_d(\theta_v) \langle \rho \rangle \quad (7)$$

(2) Choosing any pixel as the target, the reflectance of each pixel can be calculated as follows:

$$\rho_t = (\frac{\rho^*}{T_g} - \rho_a) \frac{1}{T(\theta_s) e^{-\tau/\mu_v}} - [(\frac{\rho^*}{T_g} - \rho_a) \frac{s}{T(\theta_s) e^{-\tau/\mu_v}} + \frac{t_d(\theta_v)}{e^{-\tau/\mu_v}}] \langle \rho \rangle \quad (8)$$

where the target reflectance  $\rho_t$  and equivalent environmental reflectance  $\langle \rho \rangle$  are unknown parameters.

Assuming that the selected area is a uniform region, the initial reflectance value can be computed according to Equation (1):

$$\rho_{uniform} = \frac{\frac{\rho^*}{T_g} - \rho_a}{T(\theta_s)T(\theta_v) + (\frac{\rho^*}{T_g} - \rho_a)s} \quad (9)$$

where  $\rho_{uniform}$  is the initial environmental reflectance value of each pixel.

Then, the target reflectance of each pixel can be calculated according to Equation (8):

$$\rho_t^{(0)} = \frac{\frac{\rho^*}{T_g} - \rho_a}{T(\theta_s)e^{-\tau/\mu_v}} - \left[ \frac{(\frac{\rho^*}{T_g} - \rho_a)s}{T(\theta_s)e^{-\tau/\mu_v}} + \frac{t_d(\theta_v)}{e^{-\tau/\mu_v}} \right] \rho_{uniform} \quad (10)$$

where  $\rho_t^{(0)}$  is the initial value of the target reflectance of each pixel.

However, in reality, most of the images are not uniform, that is,  $\rho_t \neq \rho_e$ . In the above assumption, each pixel is calculated as a uniform scene, that is,  $\rho_t = \rho_e$ , which will make the initial value of high reflectance higher and initial value of low reflectance lower, providing a basis for the next step.

The equivalent environmental reflectance can be regarded as the mean of all reflectance within a certain range around the target reflectance. Therefore, the equivalent environmental reflectance can be estimated as the average reflectance of the area:

$$\langle \rho(m_0, n_0) \rangle^{(0)} = \frac{1}{(N+1)^2} \sum_{m=m_0-N/2}^{m_0+N/2} \sum_{n=n_0-N/2}^{n_0+N/2} \rho(m, n)_t^{(0)} \quad (11)$$

where  $(m_0, n_0)$  is the target pixel coordinate,  $\langle \rho(m_0, n_0) \rangle^{(0)}$  is the initial value of equivalent environmental reflectance,  $(m, n)$  is the coordinate of any pixel within the area of  $(N+1) \times (N+1)$ , and  $\rho(m, n)_t^{(0)}$  is the initial value of target reflectance corresponding to  $(m, n)$ , that is,  $\rho_t^{(0)}$  is calculated by Equation (10).

In the previous step, it was mentioned that the assumption of uniform background will lead to the calculation error of reflectance. In this step, the average calculation of equivalent environmental reflectance will effectively eliminate this error and make the calculated equivalent environmental reflectance close to the real value.

Then, we use the equivalent environmental reflectance obtained in the previous step and substitute it into the calculation equation of the target reflectance (Equation (10)), in order to obtain a more accurate target reflectance, and then substitute the target reflectance into Equation (11) to obtain the equivalent environmental reflectance. After  $g$  repetitions, the equation can be expressed as follows:

$$\rho(m, n)^{(g)} = \frac{\frac{\rho^*}{T_g} - \rho_a}{T(\theta_s)e^{-\tau/\mu_v}} - \left[ \frac{(\frac{\rho^*}{T_g} - \rho_a)s}{T(\theta_s)e^{-\tau/\mu_v}} + \frac{t_d(\theta_v)}{e^{-\tau/\mu_v}} \right] \langle \rho(m, n) \rangle^{(g-1)} \quad (12)$$

The principle of this step is that all pixels in the region are not only targets, but also components of the environment. Each pixel is involved in the calculation of both the target and equivalent environment reflectance.

When  $|\rho(m, n)^{(g)} - \rho(m, n)^{(g-1)}| \leq 0.001$  is satisfied, the iteration process is stopped to obtain the reflectance of each pixel.

In the above process, there is still a problem. Inversion is for all pixels in the area. When the  $(N+1) \times (N+1)$  area is selected as the inversion object, as described above, Equation (11) can be applied to calculate the central pixel when calculating the equivalent environmental reflectance. However, when other pixels are used as the target pixels, a large enough environment cannot be selected to calculate the equivalent environmental reflectance. This means that, for the inversion area, it needs to be at least doubled to meet the demand of reflectance calculation accuracy of each pixel in the  $(N+1) \times (N+1)$  area.

This problem needs to be viewed in combination with the adjacency effect. For most land surfaces, the effective horizontal range of adjacency effects is approximately 100–500 m [13–15]. Based on this range, the effective influence distance of the adjacency effect is selected as  $N$  pixels (the distance is  $N$  multiplied by the ground sampling distance (GSD)), which is expanded once, namely, the  $(2N + 1) \times (2N + 1)$  area centered on the target pixel is selected in the image to calculate the reflectance of the  $(N + 1) \times (N + 1)$  area.

### (3) Calculation of the equivalent environmental reflectance

After calculating the reflectance of each pixel according to the above steps, it is still necessary to quantitatively analyze the influence of adjacency effect. As described in Section 2.1, the 6S radiative transfer model proposes to characterize the contribution of the target pixel to the environment by the environment function  $F(r)$ , which means the sum of the environment weighting factors of each pixel in the surrounding area is relative to the target pixel [11]. The equivalent environment reflectance is the sum of the product of the reflectance of all surrounding pixels and their corresponding weighting factors.

If the selected inversion area is large enough to cover all the environmental pixels affected by the target, the sum of the environmental weighting factors should be 1. However, in fact, this condition is often difficult to achieve, so it is necessary to evaluate the total weight of the region, in order to calculate the equivalent environmental reflectance.

Therefore, in this step, the weighting factor corresponding to each pixel in the region is calculated (Equation (13)) and combined with the environmental reflectance obtained in the previous step to calculate the equivalent environmental reflectance (Equation (15)).

The sum of weighting factors  $q(m, n)$  in the  $(N + 1) \times (N + 1)$  area is:

$$q(m, n) = \sum_{m=m_0-N/2}^{m_0+N/2} \sum_{n=n_0-N/2}^{n_0+N/2} (\Delta F(r)) \quad (13)$$

where  $\Delta F(r)$  is the weighting factor of the pixel  $(m, n)$  at  $r$  km from the central pixel  $(m_0, n_0)$ , and its functions are derived from the environmental function  $F(r)$  in the 6S radiative transfer model (subroutine ENVIRO):

$$\Delta F(r) = \frac{GSD}{2\pi\sqrt{(m-m_0)^2 + (n-n_0)^2}} \cdot \frac{\Delta F^R t_d^R + \Delta F^A t_d^A}{t_d^R + t_d^A} \quad (14)$$

where  $\Delta F^R$  is the Rayleigh weighting factor,  $t_d^R$  is the Rayleigh upward diffuse transmittance,  $\Delta F^A$  is the aerosol weighting factor, and  $t_d^A$  is the aerosol upward diffuse transmittance.

In the 6S radiative transfer model,  $F(r)$  is integrated by the weighting factor of the circle at the distance from the target  $r$  km. Considering the weighting factor corresponding to a pixel at the distance from the target  $r$  km, the weighting factor of this pixel is the product of its proportion in the circle (i.e.,  $\frac{GSD}{2\pi\sqrt{(m-m_0)^2 + (n-n_0)^2}}$ ) and the circle weight factor (i.e.,  $\frac{\Delta F^R t_d^R + \Delta F^A t_d^A}{t_d^R + t_d^A}$ ).

Thus, the equivalent environmental reflectance can be expressed as follows:

$$\langle \rho(m_0, n_0) \rangle_{eq} = \frac{1}{q(m, n)} \cdot \sum_{m=m_0-N/2}^{m_0+N/2} \sum_{n=n_0-N/2}^{n_0+N/2} (\rho(m, n) \cdot \Delta F(r)) \quad (15)$$

Then, the surface reflectance can be obtained as:

$$\rho(m_0, n_0) = \frac{\frac{\rho_s^*}{T_s} - \rho_a}{T(\theta_s)e^{-\tau/\mu_v}} - \left[ \frac{(\frac{\rho_s^*}{T_s} - \rho_a)s}{T(\theta_s)e^{-\tau/\mu_v}} - \frac{t_d(\theta_v)}{e^{-\tau/\mu_v}} \right] \langle \rho(m_0, n_0) \rangle_{eq} \quad (16)$$

Finally, the reflectance of each pixel can be calculated.

### 2.3. Radiometric Calibration-Reflectance Inversion Iterative Model

In the above process of reflectance inversion, it is worth noting that the equivalent environmental reflectance is obtained by analyzing the adjacency effect of the inversion region. In the calibration process, this is difficult to achieve, because it is impossible to measure a large area point by point. Based on this, this paper proposes a RCRII model that combines radiometric calibration and reflectance inversion in overall iteration. The iteration steps are as follows:

- (1) Radiometric calibration is conducted for the grayscale target area, and initial values of the calibration coefficient and dark current are calculated.
- (2) The reflectance inversion model described in the above section is applied to the same image to obtain the surface reflectance.
- (3) The equivalent environmental reflectance of the target area is determined with the retrieved surface reflectance and substituted into the calibration equation. The calibration coefficient and dark current are again calculated, and reflectance inversion is again performed. The iteration process is repeated a certain number of times until the relative difference between the calibration coefficient and previous iteration result is less than 1%. Notably, for  $\left| A^{(g)} - A^{(g-1)} \right| \leq 0.001 \cdot A^{(g)}$ , the iteration process is terminated. A model flow chart is shown in Figure 2.

In the calibration experiment, when the grayscale target placement site is a uniform site or relatively uniform background, the approximate value of the environmental reflectance can be obtained via site measurement. However, when the experimental area is a complex environment, the environmental reflectance cannot be acquired. Only the image count value near the target area can be used to estimate the environmental reflectance; the diffuse-to-global irradiance ratio can be obtained with the irradiance-based method to calculate the calibration parameters. The calibration inversion iterative model adopts the calculated calibration coefficient as the initial value, combined with multiple iterations of the reflectance inversion model, to increase the calibration accuracy.

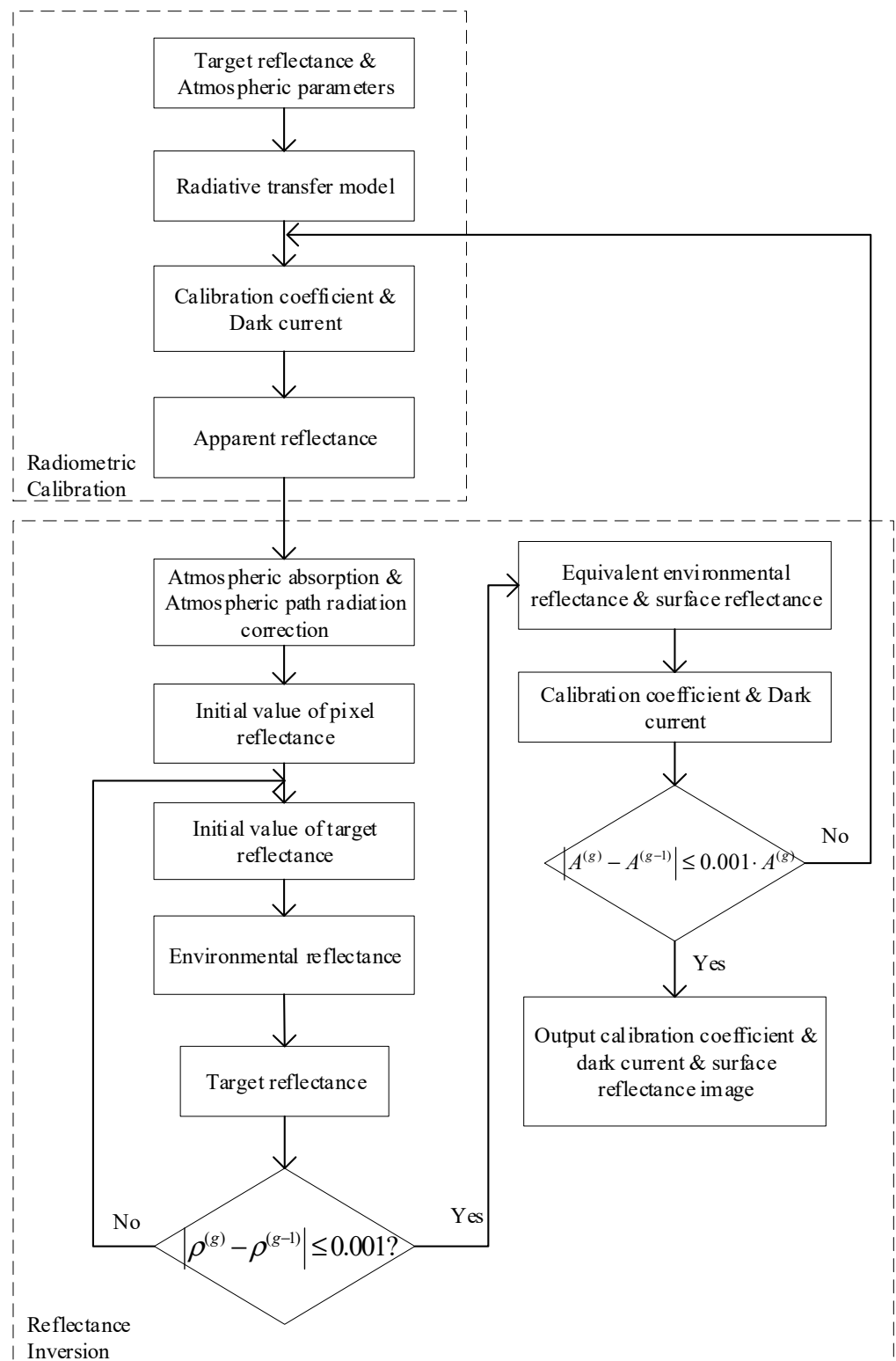
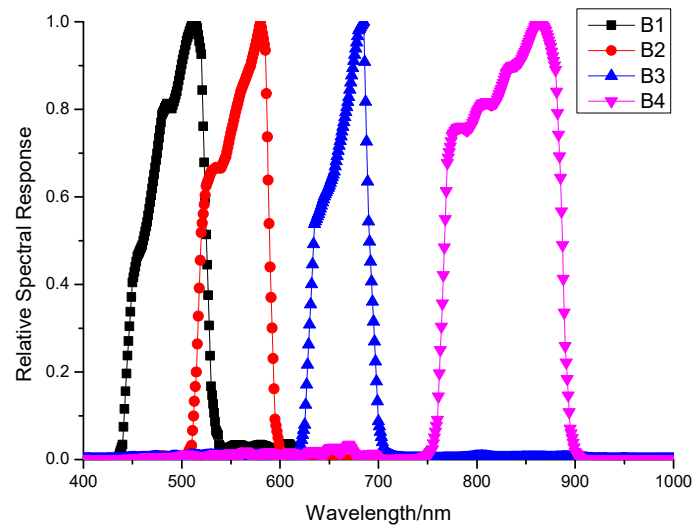


Figure 2. RCR II model flow chart.

### 3. Experiment and Data Analysis

Pakistan remote sensing satellite (PRSS-1) was successfully launched at China Jiuquan Satellite Launch Center on 9 July 2018. PRSS-1 is equipped with two panchromatic multi-spectral high-resolution cameras (PMS cameras), with pixel resolutions of 1 m panchromatic and 3 m multispectral, respectively. The camera type is TDICCD push broom type, and the imaging method is linear array push broom imaging, with a single width of about 30 km.

The width of two cameras after splicing is better than 60 km. The design life is 7 years [16]. The spectral response function of the multispectral camera is shown in Figure 3.



**Figure 3.** Relative spectral response of PRSS-1 multispectral camera.

### 3.1. Experimental Data Measurement

The Dunhuang radiometric calibration site is located 15 km west of Dunhuang City, Gansu Province, China. The surface reflectance at this site is stable, and the atmosphere is dry and clean. In August 2018, grayscale targets with reflectance levels of 5%, 20%, 40%, and 60% were placed at the site, and a calibration test was performed in regard to the high-spatial resolution multispectral camera of PRSS-1. The target placement area at the site is greater than  $10 \times 10$  pixels, and an average value of  $3 \times 3$  pixels at the center was chosen for calibration calculation to avoid the influence of the camera modulation transfer function (MTF). Recorded on 18 August 2018, the site test photo, obtained images, and site measurement parameters are as follows (Figures 4–6).



**Figure 4.** Site test photo.

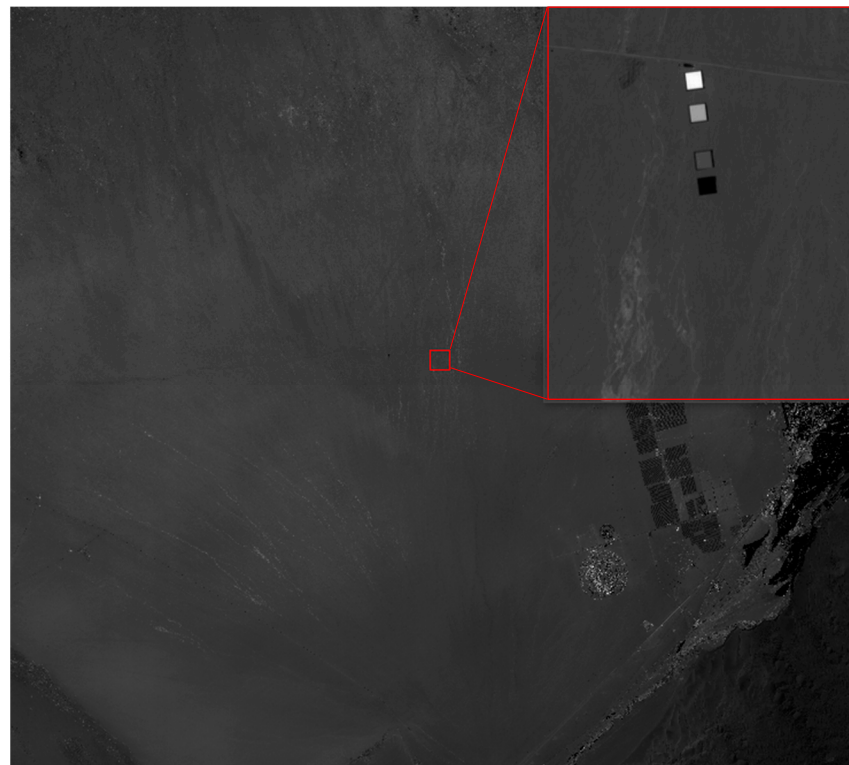


Figure 5. Multispectral image of the target area on 18 August 2018 (band 1).

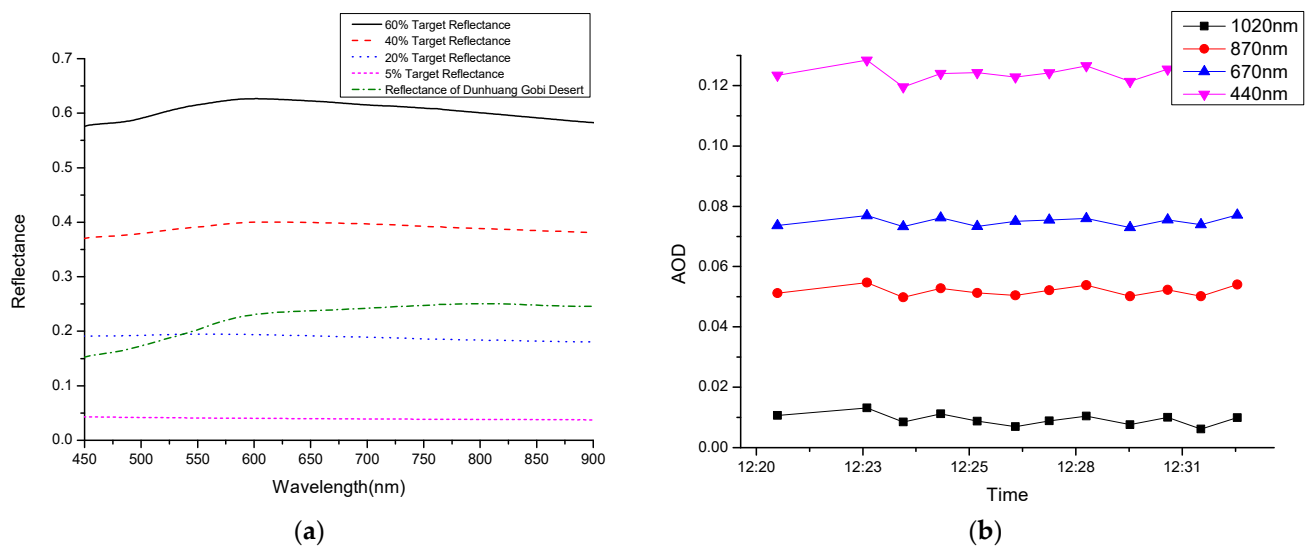


Figure 6. (a) Measured ground reflectance of the multi-grayscale targets on 18 August 2018 (overpass time: 12:28). (b) Aerosol optical depth on 18 August 2018.

The acquired image has been relatively calibrated, so the response inconsistency will not be discussed in this paper.

The spectral reflectance of the target and Gobi areas was measured with an ASD spectroradiometer and calibration panel at the time of satellite overpass. With the calibration panel, the bidirectional reflectance factor (BRF) and directional hemispherical reflectance (DHR) were determined in the laboratory, which were used to correct the solar illumination angle of the measured reflectance.

### 3.2. Calibration Calculation and Reflectance Inversion

Based on the calibration slope and intercept equation mentioned in the previous section, the measured ground reflectance of the emplaced targets was linearly regressed with the corresponding image digital numbers, as shown in Figure 7.

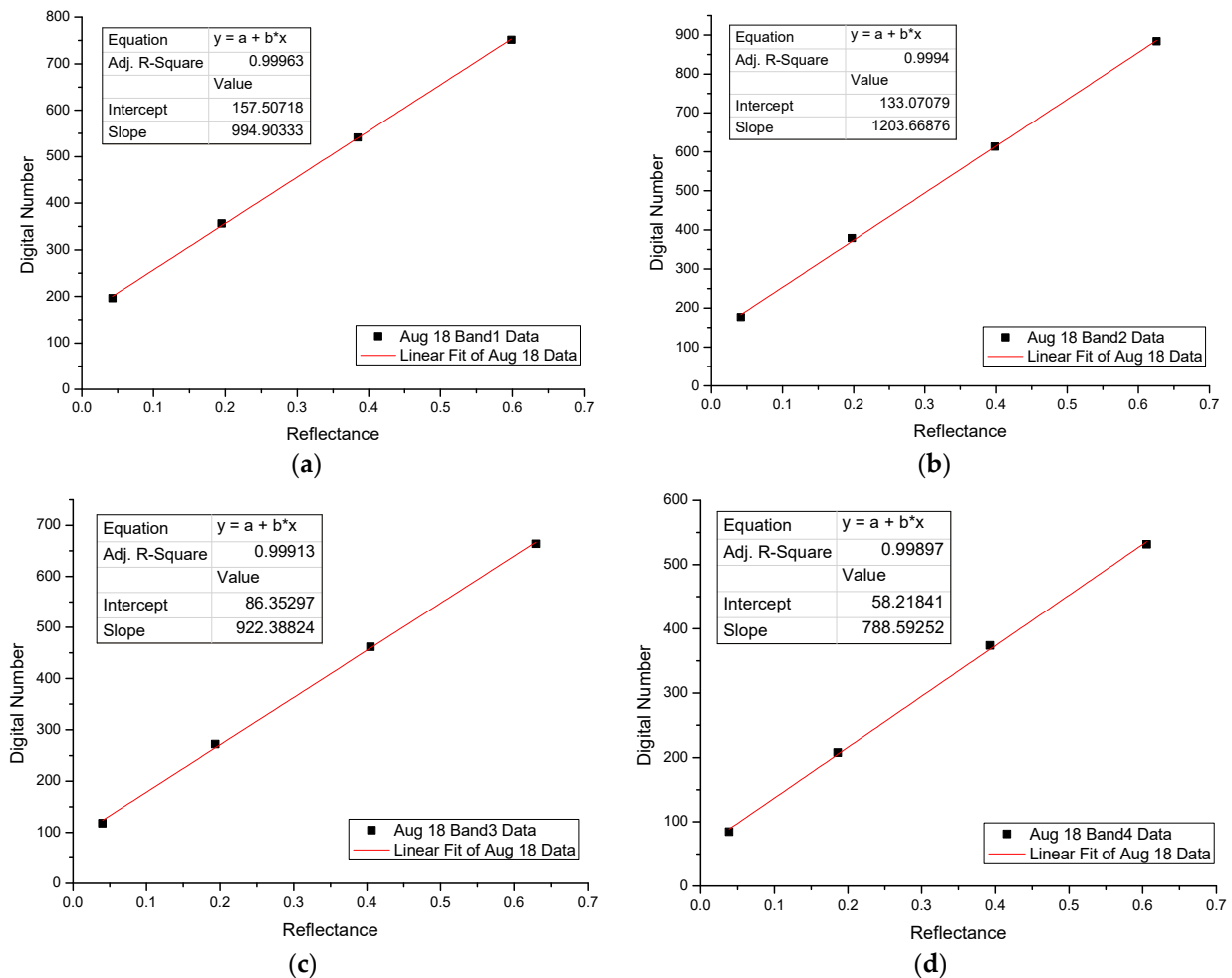


**Figure 7.** Linear regression curve between the measured ground reflectance of the multi-grayscale targets, and the corresponding image digital numbers on 18 August 2018; (a–d) show blue, green, red, and NIR bands.

Based on the measured data, the downward direct transmittance calculated with the 6S radiative transfer model was compared to the measured result of the solar photometer, and the transmittance difference remained within 0.015, as shown in Figure 8.

Combined with the above data and Equations (5) and (6), initial values of the calibration coefficient and offset could be obtained. According to Equation (6), the offset in the four bands ranged from 30~50 counts. If this parameter was not deducted and the calibration coefficient directly calculated with the uniform site calculation Equation (2), this may lead to a large difference in the calibration coefficient, which is also related to the low reflectance of the Gobi.

As described in the above section, the RCR II model was used in the test area. Considering the spatial resolution of the camera and influence of adjacency effect,  $1023 \times 1023$  pixels (corresponding to the  $(2N + 1) \times (2N + 1)$  area, mentioned in the previous section, i.e.,  $N = 511$ ) area with 60% of the target center as the central pixel is selected. After applying the RCR II model, the calculated equivalent environmental reflectance was substituted into the calibration equation for calculation purposes. After multiple iterations, the final calibration coefficient, offset, and surface reflectance results could be obtained.

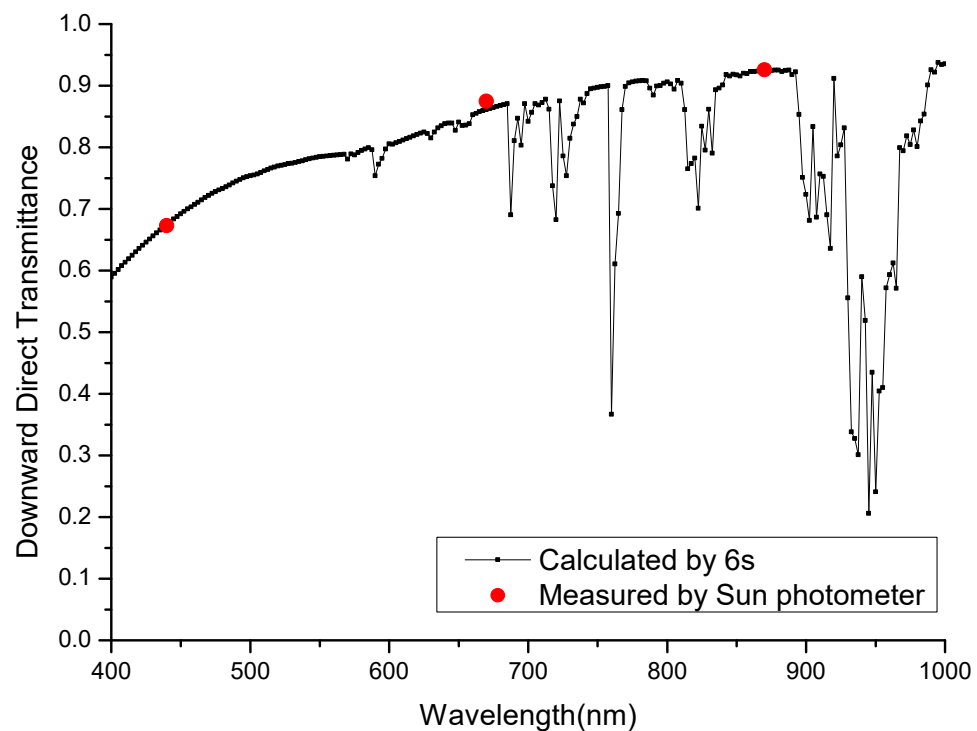


**Figure 8.** Comparison of transmittance between sun photometer measurement and 6S calculation on 18 August 2018.

The measured reflectance (that is, the reflectance measured with ASD during calibration mentioned in “Experimental Data Measurement” in Section 3.1), reflectance obtained by directly applying the initial value of the calibration coefficient (i.e., the constant calibration method), and reflectance obtained by applying the RCRII model of 60% target are compared, respectively. The results are as follows (Table 1).

**Table 1.** Comparison of the 60% target reflectance results.

	Measured Reflectance	No Model Used		RCRII Model Used	
		Inversion Reflectance	Absolute Difference	Inversion Reflectance	Absolute Difference
<b>Band 1</b>	0.599	0.591	0.00756	0.597	0.00220
<b>Band 2</b>	0.626	0.619	0.00657	0.623	0.00224
<b>Band 3</b>	0.629	0.623	0.00654	0.626	0.00356
<b>Band 4</b>	0.606	0.598	0.00737	0.600	0.00560

In Table 1, “No modal used” means that the calibration coefficient calculated by linear regression (i.e., the initial value of the calibration coefficient in the model) is directly used in the reflectance inversion model without the radiometric calibration-reflectance inversion iteration.

In summary, the absolute difference between the inversion results and measured data remained within 0.01. Additionally, it is worth emphasizing that the adjacency effect was greater at the short wavelength and smaller at the long wavelength, which is consistent with the inversion results. In band 4, due to the decrease of adjacency effect, there was almost no difference before and after the application of the model.

#### 4. Method Application

In the previous section, by comparing the measured reflectance with the inversion reflectance before and after the application of the model, it can be proven that the calibration coefficient obtained by the application of the model can correct the adjacency effect. The

apparent reflectance image can be obtained by applying the calibration coefficient obtained in the previous section to PRSS-1.

In this section, it is planned to cross-verify PRSS-1 and Sentinel-2 satellites, compare the difference of their at-sensor radiance, and compare the difference of ground reflectance through the application of reflectance inversion model, so as to evaluate the calibration accuracy.

Sentinel-2 is an Earth observation mission of the Copernicus Programme that systematically acquires optical imagery at a high spatial resolution over both land and coastal waters [17–19]. To achieve the goal of observation missions and improve the timeliness of observation data, Sentinel-2 comprises the Sentinel-2A and Sentinel-2B satellites. Through networking and collaborative observation, Sentinel-2 can realize high-frequency Earth observation with a revisit cycle of five days. Sentinel-2 provides 13 spectral channels, covering visible near-infrared to shortwave infrared bands. Visible near-infrared mainly includes four bands, namely, B2, B3, B4, and B8, with a spatial resolution of 10 m. The spectral response function is shown in Figure 9.

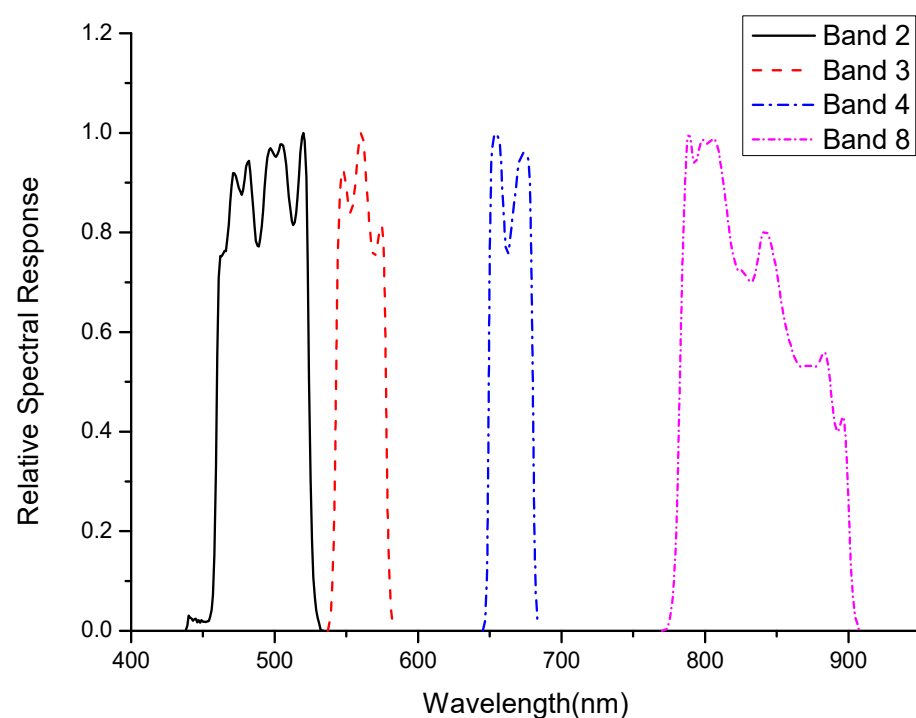


**Figure 9.** Sentinel-2A relative spectral response.

To verify the reliability of the proposed model, cross-validation and reflectance inversion were conducted with the Sentinel-2A and PRSS-1 image data obtained on 18 August 2018. The imaging time difference between these satellites was less than 10 min, and the weather was good on that day. The aerosol optical depth for 550 nm was 0.0936. The observed zenith angle was lower than 10 degrees.

The central wavelengths of the Sentinel-2A and PRSS-1 visible near-infrared bands are as follows (Table 2).

**Table 2.** PRSS-1 and Sentinel-2A band center wavelength (nm).

PRSS-1 Band/Sentinel-2A Band	PRSS-1	Sentinel-2A
Band1/Band2	496.165	492.437
Band2/Band3	557.375	559.849
Band3/Band4	664.622	664.622
Band4/Band8	823.127	832.794

#### 4.1. Top-of-Atmosphere Radiance Cross-Validation

The Gobi near the target is selected as the cross-validation object. Since the spectral response functions of the two satellites are inconsistent, it is necessary to calculate the spectral matching factor before cross-validation. The process is as follows:

- (1) Using 6S radiative transfer model and field measurement parameters, the at-sensor radiance of the two satellites  $L_{6S-S2}$ ,  $L_{6S-PRSS1}$  is calculated, respectively; then, the spectral matching factor can be obtained as the ratio of the two.
- (2) Take the Gobi on the east side of the target as the crossing object; the PRSS-1 calibration coefficient and offset obtained in the above section is used to calculate the at-sensor radiance by  $L_{PRSS1} = \frac{\mu_s E_s}{\pi} \frac{DN_{Gobi} - DN_0}{A}$ . The at-sensor radiance of Sentinel-2A  $L_{S2}$  is directly obtained from the L1C level image.
- (3) The at-sensor radiance of PRSS-1  $L_{PRSS1-cross}$  is converted by spectral matching factor and compared with Sentinel-2A.

According to the above process, the results are as follows (Table 3).

**Table 3.** Cross-validation results of PRSS-1 and Sentinel-2A.

PRSS-1 Band/Sentinel-2A Band	Spectral Matching Factor	$L_{PRSS1-cross}$	$L_{S2}$	Relative Deviation (%)
Band1/Band2	1.019	101.945	101.040	0.892
Band2/Band3	1.028	103.742	100.241	3.432
Band3/Band4	1.038	97.504	94.385	3.251
Band4/Band8	1.000	67.611	65.427	3.283

The results of cross-validation show that the difference in radiance between PRSS-1 and Sentinel-2A is within 3.5%.

#### 4.2. Reflectance Inversion Verification

It can be seen from Table 2 that the spectrum and bandwidth of these two satellites are inconsistent, but the central wavelengths are similar. Theoretically, it is necessary to reconstruct the reflectance obtained via inversion and then compare the results. However, according to the spectra of the selected three areas (Gobi, grassland, and water areas), the absolute difference in reflectance, due to the inconsistency in spectral response functions between Sentinel-2A and PRSS-1, should occur within 0.005. Therefore, the reflectance inversion results were directly compared here. A water/Gobi area with the Dunhuang Gobi as a uniform background and water/grassland area with Dunhuang City, as a complex environmental background was selected. The selected area images (from PRSS-1) are as follows (Figures 10–13).

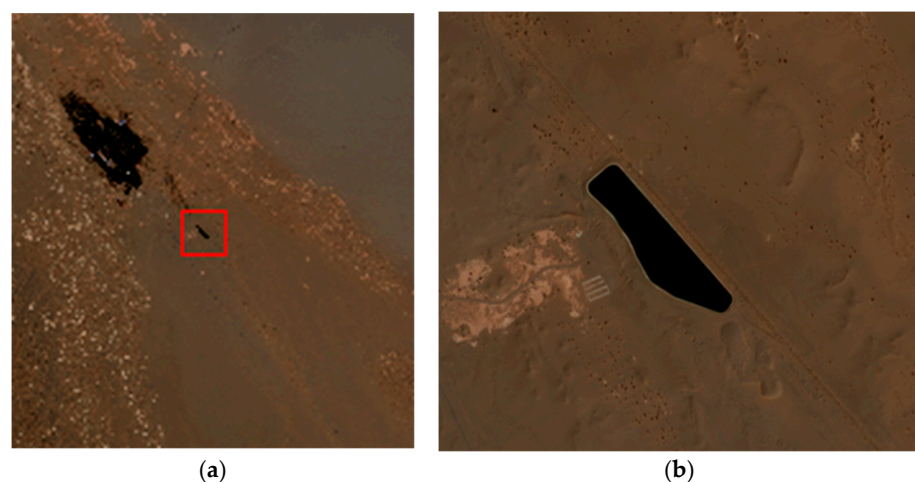


**Figure 10.** (a) Select Water1 area (in the red box) and its surrounding environment (Gobi background); (b) enlarged Water1 area (the area is about  $(76.48 \times 128.06) \text{ m}^2$ ).

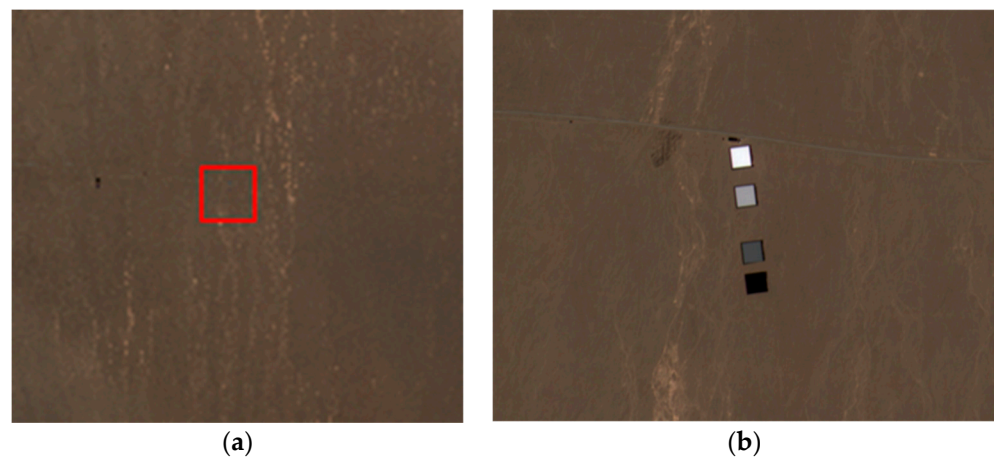


**Figure 11.** (a) Select Gobi area (in the red box) and its surrounding environment; (b) enlarged Gobi area (near the target).

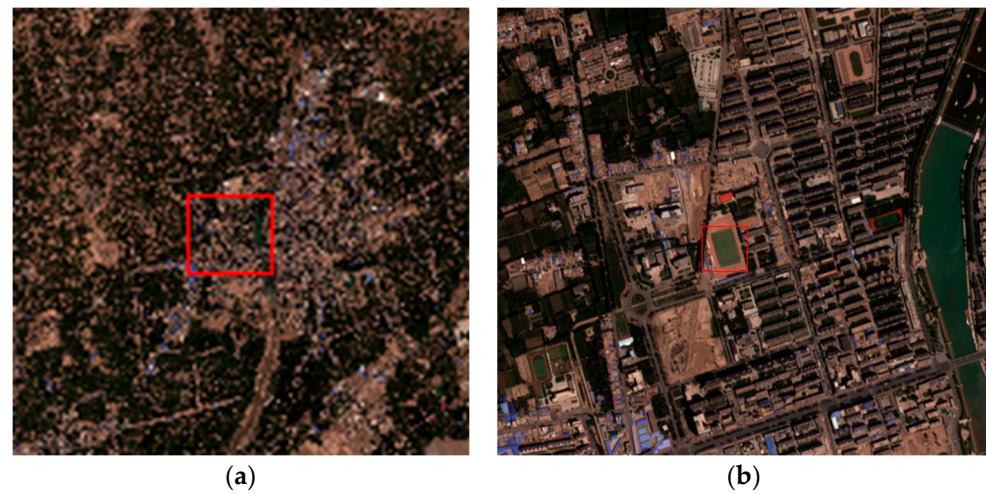


**Figure 12.** (a) Select Grassland area (in the red box) and its surrounding environment (urban background); (b) enlarged Grassland area (the area is about  $(63.57 \times 112.09) \text{ m}^2$ ).

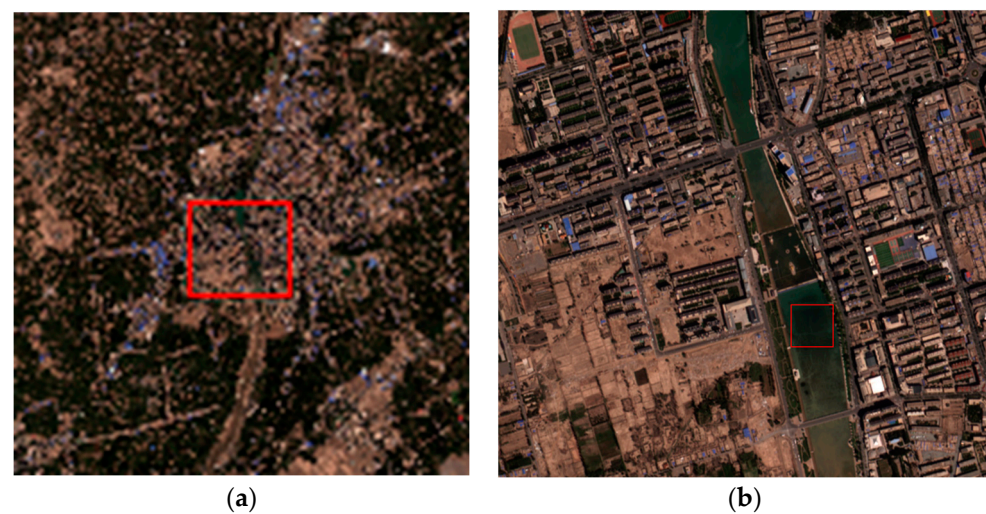


**Figure 13.** (a) Select Water2 area (in the red box) and its surrounding environment (urban background); (b) enlarged Water2 area.

Using the Sentinel-2 L1C level image, the obtained apparent reflectance was input into the reflectance inversion model proposed in this paper, so as to obtain the ground reflectance results. It was compared with the ground reflectance results of PRSS-1, which was directly applied to the RCRII model. These results are shown in Figures 14 and 15.

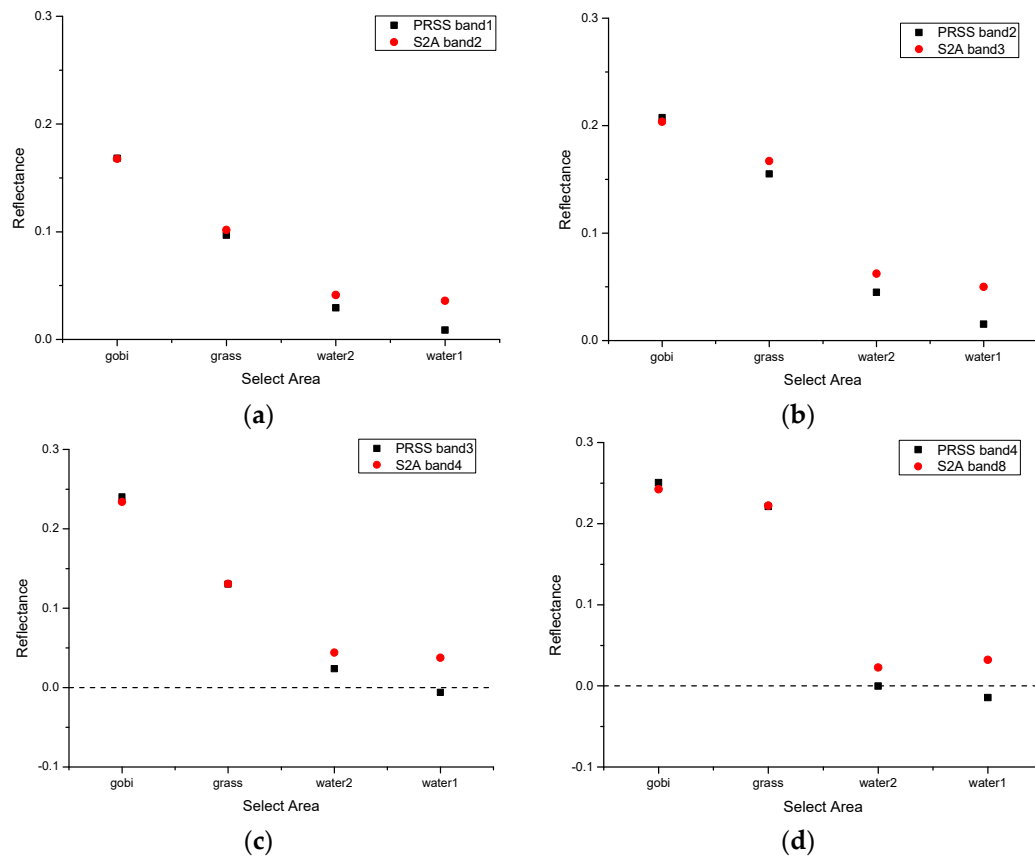


**Figure 14.** Comparison of ground reflectance in different areas obtained by PRSS-1 using RCRII model and Sentinel-2 using reflectance inversion model; (a–d) show blue, green, red, and NIR bands.

The inversion results of the Gobi area were compared to the measured values. It can be seen from Figure 16 that the ground Gobi reflectance measured by ASD is compared with the results of PRSS-1 using the RCRII model and reflectance inversion results of Sentinel-2A. The result of PRSS-1 is closer to the measured reflectance. For reflectance inversion, it should be more convincing to take the actual measured reflectance of the site as the standard; however, due to the lack of measured data, only the comparison of Gobi reflectance is given here. Considering that the difference of the inversion results of Sentinel-2A is greater than PRSS-1, it is only for comparison and reference in the follow-up, and quantitative analysis will not be carried out.

According to the above results, the reflectance retrieved by Sentinel-2A and PRSS-1 was close in the Gobi and grassland areas, and the difference remained within 0.01. However, there occurred a large reflectance difference in the two selected water areas. The reflectance retrieved by Sentinel-2A in the water area was obviously high, and a 3~4% reflectance was obtained in the near-infrared band. Inversion of PRSS-1 in the Water1 area yielded a negative value in the near-infrared band. There are many possible reasons for this phenomenon, i.e., the model error of reflectance inversion, estimation error of offset, and so on. Most importantly, too little data makes it difficult to obtain statistical results. Therefore, the specific reason still needs further analysis and the determination of more data.

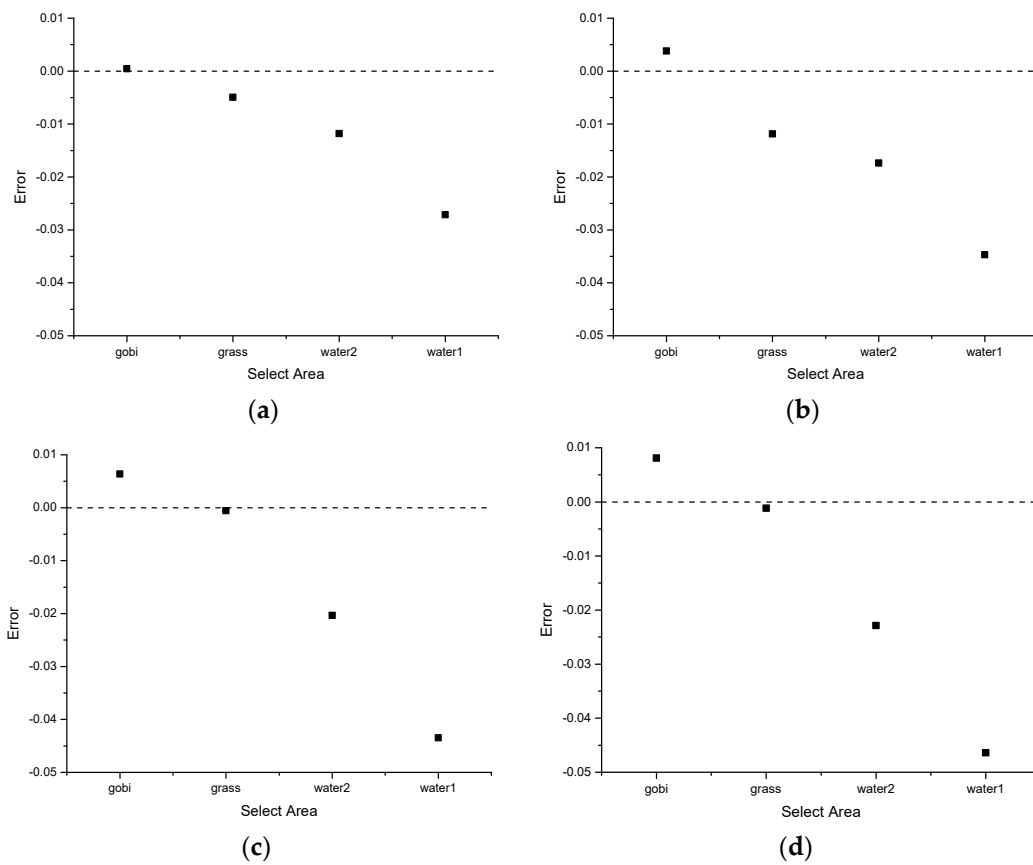


**Figure 15.** Comparison of absolute difference of ground reflectance in different areas obtained by PRSS-1 using RCRII model and Sentinel-2 using reflectance inversion model; (a–d) show blue, green, red, and NIR bands.

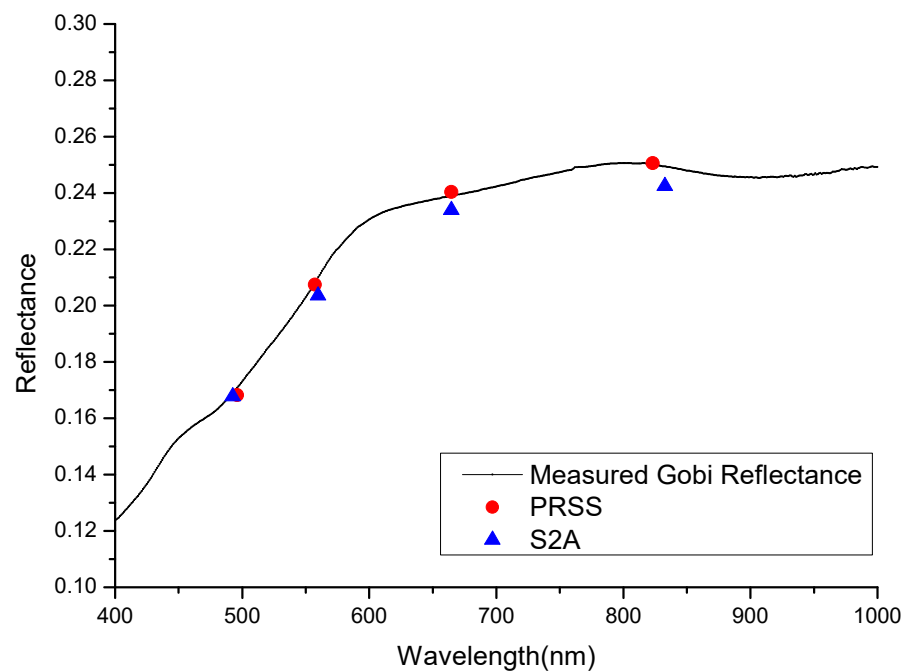


**Figure 16.** Comparison between the Gobi ground reflectance obtained by PRSS-1 using RCRII model and Sentinel-2 using the reflectance inversion model and measured Gobi reflectance by ASD.

## 5. Discussion

The RCR II model is mainly composed of two parts: radiometric calibration and reflectance inversion. For the radiometric calibration method, the grayscale target calibration method is selected because the camera may have offset, which will lead to large errors in the calibration of uniform site with low reflectance. The linear regression of multiple reflectance targets can separate the target radiation from the non-target radiation (i.e., atmospheric path and environmental radiation), calculate the calibration coefficient with the target radiation, and calculate the offset with the non-target radiation. However, the multi-grayscale target calibration method needs to consider the influence of adjacency effect. The actual measurement obviously cannot meet the requirements of adjacency effect range, and it is difficult to measure point by point to quantify its influence. Therefore, on this basis, the reflectance inversion model is introduced to form the radiometric calibration-reflectance inversion iterative model in this paper. In addition, there are still several problems to discuss.

In the third section, the selected area is centered on the 60% target, and the inversion results of the 60% target are also discussed. However, for the multi-grayscale target method, the most appropriate method should be to evaluate the combined errors of four targets (60%, 40%, 20%, and 5%). The reason this is not achieved is due to the adjacency effect. The influence of adjacency effect on target method is reflected in the variable of equivalent environmental reflectance, which can be divided into two parts: the influence on the linearity and nonlinearity of the target. This can be seen in Equations (5) and (6) in Section 2. When we use the linear regression method to realize the target calibration, the influence of adjacency effect on nonlinearity has been ignored. However, in fact, for targets with different reflectance, the equivalent environmental reflectance is a variable. Back to the original problem, in the application of the model centered on the 60% target, the evaluation of the equivalent environmental reflectance is completely determined by the 60% target. This assumption may lead to unexpected errors in other reflectance targets. Fortunately, when the aerosol optical thickness is small, the error caused by this factor can be ignored (this can be seen from the inversion error, but the difference can still be observed in the model). However, when the aerosol optical thickness is large and adjacency effect is more obvious, this error is difficult to ignore. Therefore, the model may need to improve this part. However, it should be emphasized that, even if such errors exist in the model, it can still effectively eliminate the adjacency effect.

Another problem is that, in the example provided in this paper, the target was deployed under the background of a uniform site. In fact, in the principles described in Section 2, there are no special requirements for the environment. In other words, this model should be able to be implemented, even in complex environments. The difficulty of complex environment lies in how to obtain the initial value of environmental reflectance to calculate the initial value of calibration coefficient. This problem can be substituted into the model by calculating the initial value of reflectance by selecting the mean value of the area or obtaining the ratio of diffuse-to-global by irradiance-based method. Unfortunately, due to the lack of data, it is difficult to prove this point at present. Try to substitute 0.5 and 0.01 as the initial values of environmental reflectance into the model, and still get good inversion results; however, this fact is still difficult to prove its universality in complex environments.

In regard to the grayscale target calibration method, the uncertainty mainly originates from two sources: (1) the target reflectance-image digital number fitting error, which can be divided into the nonlinear error of the camera sensor, reflectance measurement uncertainty, and uncertainty due to the inconsistent influence of the adjacency effect attributed to varying target reflectance values; (2) the error in the radiative transfer model during atmospheric parameter calculation.

Therefore, in addition to the above two factors and the measurement error of the instrument, the influencing factors can be summarized as the calculation of the total ground irradiance, measurement of the bidirectional reflection distribution function (BRDF) of the target, calculation of the upward atmospheric transmittance, and adjacency effect.

The uncertainty of the total ground irradiance mainly comes from the radiative transfer model, and the uncertainty of the radiative transfer model mainly comes from the assumptions of the aerosol model and calculation of the solar irradiance. Therefore, it is considered that the uncertainty is less than 3%. The grayscale target has the characteristics of constant spectrum and near-Lambertian. Therefore, it is considered that the BRDF measurement uncertainty is less than 2%. The uncertainty of upward atmospheric transmittance mainly comes from aerosol scattering. The parameters in radiation transmission can be calculated by using the Langley method to calculate the atmospheric optical thickness measured by the sun photometer. The uncertainty of atmospheric optical thickness measurement mainly comes from the calibration of the sun photometer, and the measurement uncertainty is less than 2%.

To sum up, compared with the conventional calibration methods, we expect to use the RCRII model to calculate sensor offset, improve the reflectance measurement accuracy, and quantitatively analyze the impact of adjacency effect, so as to improve calibration accuracy. A preliminary assessment of the uncertainty of this method is made, as shown in Table 4. This part will be further analyzed later.

**Table 4.** Uncertainty analysis for the vicarious calibration using RCRII model.

Uncertainty Factors	Relative Uncertainty (%)
Calculation of total ground irradiance	3.0
Target BRDF measurement	2.0
Calculation of upward transmittance	2.0
Adjacency effect calculation	1.0
Others (geometric factors, etc.)	1.0
Comprehensive uncertainty	4.4

## 6. Conclusions

Radiometric calibration and reflectance inversion are usually independent processes. Generally, calibration is followed by reflectance inversion. In this paper, a general iterative model for radiometric calibration-reflectance inversion, based on the 6S radiative transfer method, was proposed. The two processes of radiometric calibration and reflectance inversion were combined, and calibration and inversion of the same image were repeated in an iterative process to improve the accuracy. The equivalent environmental reflectance calculated with the inversion model was applied in calibration, and the calibration results were again used for inversion. Via a comparison to the measured values in the calibration experiment, calibration and inversion integration was achieved, and quantitative remote sensing was preliminarily realized. With the use of the proposed model against the background of the Dunhuang uniform site, the results indicated that the difference between the reflectance obtained with the established method and measured reflectance was less than 0.01. By comparing with Sentinel-2a image, it is cross-verified that the radiance difference was within 4%, and the difference between the inversion value and measured value remained below 0.01 in the range of 0.1~0.3 reflectance, and the reason for the large difference at a low reflectance was analyzed.

In fact, this model is more inclined to be applied in complex environments or situations with large adjacency effects. However, due to the lack of data, it is difficult to prove this now. The follow-up work will focus on this part.

**Author Contributions:** S.B. was responsible for the data analysis and writing the manuscript. H.C. led the experiment and participated in data processing. L.Z. contributed to the main research ideas. W.H., X.S. and X.W. (Xianhua Wang) reviewed the manuscript and provided valuable suggestions. Y.L., Z.F., Y.C., X.W. (Xinrong Wang) and X.Z. provided image data and valuable suggestions. All authors have read and agreed to the published version of the manuscript.

**Funding:** This research received no external funding.

**Data Availability Statement:** Not applicable.

**Acknowledgments:** The Sentinel image data were downloaded from the ESA website (<https://scihub.copernicus.eu/dhus/#/home>, accessed on 8 September 2021).

**Conflicts of Interest:** The authors declare no conflict of interest.

## References

1. Yoon, H.; Kacker, R. *Guidelines for Radiometric Calibration of Electro-Optical Instruments for Remote Sensing: Handbook (NIST HB)*; National Institute of Standards and Technology: Gaithersburg, MD, USA, 2015.
2. Tan, K.; Wang, X.; Niu, C.; Wang, F.; Du, P.; Sun, D.X.; Yuan, J.; Zhang, J. Vicarious Calibration for the AHSI Instrument of Gaofen-5 With Reference to the CRCS Dunhuang Test Site. *IEEE Trans. Geosci. Remote Sens.* **2020**, *59*, 3409–3419. [[CrossRef](#)]
3. Chander, G.; Markham, B.L.; Barsi, J.A. Revised Landsat-5 Thematic Mapper Radiometric Calibration. *IEEE Geosci. Remote Sens. Lett.* **2007**, *4*, 490–494. [[CrossRef](#)]
4. Ma, L.; Zhao, Y.; Woolliams, E.R.; Dai, C.; Wang, N.; Liu, Y.; Li, L.; Wang, X.; Gao, C.; Li, C.; et al. Uncertainty Analysis for RadCalNet Instrumented Test Sites Using the Baotou Sites BTCN and BSCN as Examples. *Remote Sens.* **2020**, *12*, 1696. [[CrossRef](#)]
5. Bouvet, M.; Thome, K.; Berthelot, B.; Bialek, A.; Czaplá-Myers, J.; Fox, N.P.; Goryl, P.; Henry, P.; Ma, L.; Marcq, S.; et al. RadCalNet: A Radiometric Calibration Network for Earth Observing Imagers Operating in the Visible to Shortwave Infrared Spectral Range. *Remote Sens.* **2019**, *11*, 2401. [[CrossRef](#)]
6. Pinto, C.T.; Xin, J.; Leigh, L. Evaluation Analysis of Landsat Level-1 and Level2 Data Products Using In Situ Measurements. *Remote Sens.* **2020**, *12*, 2597. [[CrossRef](#)]
7. Yeom, J.-M.; Hwang, J.; Jung, J.-H.; Lee, K.-H.; Lee, C.-S. Initial Radiometric Characteristics of KOMPSAT-3A Multispectral Imagery Using the 6S Radiative Transfer Model, Well-Known Radiometric Tarps, and MFRSR Measurements. *Remote Sens.* **2017**, *9*, 130. [[CrossRef](#)]
8. Slater, P.N. Radiometric considerations in remote sensing. *Proc. IEEE* **1985**, *73*, 997–1011. [[CrossRef](#)]
9. Sun, B.; Schäfer, M.; Ehrlich, A.; Jäkel, E.; Wendisch, M. Influence of atmospheric adjacency effect on top-of-atmosphere radiances and its correction in the retrieval of Lambertian surface reflectivity based on three-dimensional radiative transfer. *Remote Sens. Environ.* **2021**, *263*, 112543. [[CrossRef](#)]
10. Ma, L.; Wang, N.; Liu, Y.; Zhao, Y.; Han, Q.; Wang, X.; Woolliams, E.R.; Bouvet, M.; Gao, C.; Li, C.; et al. An In-Flight Radiometric Calibration Method Considering Adjacency Effects for High-Resolution Optical Sensors Over Artificial Targets. *IEEE Trans. Geosci. Remote Sens.* **2021**, *60*, 1–13. [[CrossRef](#)]
11. Vermote, E.F.; Tanré, D.; Deuze, J.L.; Herman, M.; Morcette, J.J. Second simulation of a satellite signal in the solar spectrum-vector (6SV). In *6S User Guide Version*; IEEE: Piscataway, NJ, USA, 2006; Volume 3, pp. 1–55.
12. Slater, P.N.; Biggar, S.F.; Thome, K.J.; Gellman, D.I.; Spyak, P.R. Vicarious radiometric calibrations of EOS sensors. *J. Atmos. Ocean. Technol.* **1996**, *13*, 349–359. [[CrossRef](#)]
13. Wang, T.; Du, L.; Yi, W.; Hong, J.; Zhang, L.; Zheng, J.; Li, C.; Ma, X.; Zhang, D.; Fang, W.; et al. An adaptive atmospheric correction algorithm for the effective adjacency effect correction of submeter-scale spatial resolution optical satellite images: Application to a WorldView-3 panchromatic image—ScienceDirect. *Remote Sens. Environ.* **2021**, *259*, 112412. [[CrossRef](#)]
14. Richter, R. A fast atmospheric correction algorithm applied to Landsat TM images. *Int. J. Remote Sens.* **1990**, *11*, 159–166. [[CrossRef](#)]
15. Kaufman, Y.J. Solution of the equation of radiative transfer for remote sensing over nonuniform surface reflectivity. *J. Geophys. Res.* **1982**, *87*, 4137–4147. [[CrossRef](#)]
16. Yan, L.; Hongyao, C.; Zhou, F.; Longfei, L.; Yuanwei, C.; Yongli, H.; Hongqiang, W.; Song, W. On-orbit radiometric calibration and accuracy analysis in dual camera of PRSS-1 Satellite. *Spacecr. Recovery Remote Sens.* **2019**, *40*, 77–88.
17. Gascon, F.; Bouzinac, C.; Thépaut, O.; Jung, M.; Francesconi, B.; Louis, J.; Lonjou, V.; Lafrance, B.; Massera, S.; Gaudel-Vacaresse, A.; et al. Copernicus Sentinel-2 Calibration and Products Validation Status. *Remote Sens.* **2016**, *9*, 584. [[CrossRef](#)]
18. Lonjou, V.; Lachéradé, S.; Fougne, B.; Gamet, P.; Marcq, S.; Raynaud, J.L.; Tremas, T. Sentinel-2/MSI absolute calibration: First results. In Proceedings of the SPIE Remote Sensing, Toulouse, France, 21–24 September 2015; International Society for Optics and Photonics: Bellingham, WA, USA, 2015.
19. Angal, A.; Xiong, X.; Shrestha, A. Cross-Calibration of MODIS Reflective Solar Bands with Sentinel 2A/2B MSI Instruments. *IEEE Trans. Geosci. Remote Sens.* **2020**, *58*, 5000–5007. [[CrossRef](#)]